




ARTICLE

DOI: 10.1038/s41467-018-06043-1

OPEN

# Dendritic defect-rich palladium-copper-cobalt nanoalloys as robust multifunctional non-platinum electrocatalysts for fuel cells

Chaozhong Li <sup>1,2</sup>, Qiang Yuan <sup>1,2</sup>, Bing Ni<sup>2</sup>, Ting He<sup>2</sup>, Siming Zhang<sup>2</sup>, Yong Long<sup>2</sup>, Lin Gu <sup>3</sup> & Xun Wang<sup>2</sup>

Recently, the development of high-performance non-platinum electrocatalysts for fuel cell applications has been gaining attention. Palladium-based nanoalloys are considered as promising candidates to substitute platinum catalysts for cathodic and anodic reactions in fuel cells. Here, we develop a facile route to synthesize dendritic palladium-copper-cobalt trimetallic nanoalloys as robust multifunctional electrocatalysts for oxygen reduction and formic acid oxidation. To the best of our knowledge, the mass activities of the dendritic Pd<sub>59</sub>Cu<sub>30</sub>Co<sub>11</sub> nanoalloy toward oxygen reduction and formic acid oxidation are higher than those previously reported for non-platinum metal nanocatalysts. The Pd<sub>59</sub>Cu<sub>30</sub>Co<sub>11</sub> nanoalloys also exhibit superior durability for oxygen reduction and formic acid oxidation as well as good antimethanol/ethanol interference ability compared to a commercial platinum/carbon catalyst. The high performance of the dendritic Pd<sub>59</sub>Cu<sub>30</sub>Co<sub>11</sub> nanoalloys is attributed to a combination of effects, including defects, a synergistic effect, change of *d*-band center of palladium, and surface strain.

<sup>1</sup>College of Chemistry and Chemical Engineering, Guizhou University, Guiyang, Guizhou Province 550025, China. <sup>2</sup>Key Lab of Organic Optoelectronics and Molecular Engineering, Department of Chemistry, Tsinghua University, Beijing 100084, China. <sup>3</sup>Chinese Academy of Sciences and Beijing National Laboratory for Condensed Matter Physics, Beijing 100190, China. Correspondence and requests for materials should be addressed to Q.Y.(email: [qyuan@gzu.edu.cn](mailto:qyuan@gzu.edu.cn)) or to X.W.(email: [wangxun@mail.tsinghua.edu.cn](mailto:wangxun@mail.tsinghua.edu.cn))

Fuel cells (FCs) are efficient, clean, and sustainable energy generation units that produce electricity from fuels such as hydrogen, formic acid, methanol, and ethanol<sup>1–3</sup>. Platinum (Pt) is widely applied as a catalyst for anode and cathode reactions in FCs<sup>4–8</sup>, but many factors, including high cost that accounts for over 55% of the total cost<sup>9</sup>, scarcity, poor durability, and sluggish reaction kinetics of the oxygen reduction reaction (ORR), tremendously impede the commercial application of FCs. Therefore, developing highly effective non-Pt alloy catalysts for FCs has aroused great interest and concern of researchers from all over the world since such alloys can enhance the catalytic performance through optimizing the binding energy between reactants, intermediates and products with the alloy surface at the nanoscale<sup>10–13</sup>. For instance, Linic's group, Yoo's group, and Yang's group, respectively reported Ag–Co alloy, Rh–Sn alloy, Pd–Rh alloy, and Au–Rh alloy catalysts for electrochemical ORR in basic media<sup>14–18</sup>. However, most of the mass activities reported on non-Pt metal catalysts are below 0.20 A mg<sup>−1</sup> for ORR, which is still far from the target (0.44 A mg<sup>−1</sup><sub>Pt</sub> at 0.9 V reversible hydrogen electrode (RHE)) of the U.S. Department of Energy<sup>19</sup>. Besides activities, the alcohol (methanol or ethanol) tolerance of metal catalysts is an important concern for direct alcohol (methanol or ethanol) FCs since these fuel molecules generally penetrate the polymer electrolyte membrane and diffuse from the anode to the cathode, which will greatly lower the performance and efficiency of metal catalysts. However, no alcohol tolerance experiments were mentioned on aforementioned non-Pt metal catalysts.

Among non-Pt multimetallic electrocatalysts, Pd-based electrocatalysts have received ample attention for organic molecular oxidation and ORR<sup>20–39</sup>. Previous reports have shown that Pd-based nanoalloys can exhibit superior catalytic performance relative to Pt catalysts for FC applications<sup>40–43</sup>. As we know, the size, composition and complex shape (e.g., a dendritic shape) can be used to tune the electrocatalytic performance of Pd-based catalysts. Furthermore, many parameters, such as Pd–Pd interatomic distance, the number of Pd nearest neighbors, the *d*-band center of Pd and the Pd content on the nanoalloy surface, will change when Pd alloys with 3*d* transition metals<sup>10,12,13</sup>. Therefore, rational regulation of these parameters can boost the catalytic activity and/or durability of Pd-based nanocatalysts for ORR and/or small organic molecular oxidation. For instance, Han's group<sup>40</sup> and Huang's group<sup>43</sup> have, respectively, displayed PdCuCo anisotropic structure and ordered spherical PdCuCo with mass activities at 0.9 V versus RHE of 0.18 and 0.13 A mg<sup>−1</sup><sub>Pd</sub> for ORR, but no alcohol tolerance experiments were mentioned. Xing's group has reported that the mass activity (MA) of palladium–cobalt phosphorus/carbon (Pd–CoP/C) is 2.757 A mg<sup>−1</sup><sub>Pd</sub> toward formic acid oxidation (FAO)<sup>21</sup>. Zhang's group has reported that 4H/face-centered cubic (fcc) Au@Pd core–shell nanorods exhibit high activity toward ethanol oxidation (EO)<sup>24</sup>. However, to the best of our knowledge, there is no report on the synthesis of trimetallic PdCuCo dendritic nanoalloys as robust multifunctional electrocatalysts for both ORR and FAO.

Herein, we report a facile synthesis of trimetallic PdCuCo dendritic nanoalloys with abundant defects. The electrocatalytic performance of these as-synthesized dendritic PdCuCo nanoalloys toward ORR and FAO has been investigated. Compared with commercial Pt/C or Pd black, the dendritic Pd<sub>59</sub>Cu<sub>30</sub>Co<sub>11</sub> nanoalloys demonstrate much higher MA and durability. Besides, the dendritic Pd<sub>59</sub>Cu<sub>30</sub>Co<sub>11</sub> nanoalloys also exhibit high alcohol (methanol or ethanol) tolerance compared with commercial Pt/C. Thus, this approach provides an effective route for fabricating dendritic PdCuCo nanoalloys as robust multifunctional electrocatalysts for ORR and FAO by creating abundant defects.

## Results

**Structural characterization.** Figure 1a, b and Supplementary Fig. 1a showed the representative transmission electron microscopy (TEM) images of the as-synthesized Pd<sub>59</sub>Cu<sub>30</sub>Co<sub>11</sub> nanocrystals (the composition was determined by the inductively coupled plasma optical emission spectrometry (ICP–OES), Supplementary Table 1). As can be seen, the obtained products were of uniform size of 66.25 ± 4.5 nm (Supplementary Fig. 1b) and displayed dendritic shapes. These dendritic particles were assembled with dozens of small grains, and the size of most small grains was sub-5.0 nm, around 4.28 nm (Supplementary Fig. 1c). Well-resolved lattice fringes (Fig. 1c) are observed in the sub-5.0 nm grains and the lattice distance of 0.217 nm is very closed to the (111) interplanar distance of face-centered cubic (*fcc*) Pd. The energy dispersive X-ray spectroscopy data of one single dendritic particle showed that the as-synthesized dendritic particle consists of Pd, Cu, and Co (Supplementary Fig. 1d). The X-ray diffraction (XRD) patterns (Supplementary Fig. 1e) of the as-synthesized Pd<sub>59</sub>Cu<sub>30</sub>Co<sub>11</sub> nanocrystals showed four peaks located at 40.45, 47.05, 68.70, and 81.85° 2θ that can be indexed to (111), (200), (220), and (311) planes of the *fcc* Pd (JCPDS-46-1403)<sup>44</sup>, respectively. The diffraction pattern is not characteristic of *fcc* Cu (JCPDS-04-0836)<sup>23</sup> and *fcc* Co (JCPDS-15-0806)<sup>45</sup> phases. The peak positions of Pd<sub>50</sub>Cu<sub>50</sub>, Pd<sub>88</sub>Co<sub>12</sub>, and Pd<sub>59</sub>Cu<sub>30</sub>Co<sub>11</sub> are shifted to higher angles relative to those of the pure Pd crystal (JCPDS-46-1403), indicating that the smaller Cu and Co atoms are incorporated into the Pd lattice. According to the XRD patterns and the Debye–Scherrer equation<sup>46</sup> (Table 1), Cu and/or Co entering the Pd lattice can induce lattice contraction and strain variation, and the strain variations of trimetallic PdCuCo nanoalloys (Pd<sub>59</sub>Cu<sub>30</sub>Co<sub>11</sub>:3.50%; Pd<sub>56</sub>Cu<sub>38</sub>Co<sub>6</sub>:2.56%; Pd<sub>62</sub>Cu<sub>16</sub>Co<sub>22</sub>:2.11%) are higher than that of bimetallic Pd<sub>50</sub>Cu<sub>50</sub> (1.62%) and Pd<sub>88</sub>Co<sub>12</sub> (0.72%), which indicates that simultaneously introducing Cu and Co atoms should result in greater strain variation than introducing only Cu or Co in current system and would enhance catalytic performance of nanocrystals<sup>12,13,39,40,43</sup>. The results of XRD indicated the formation of Pd, Cu, and Co nanoalloys. Moreover, the nanoalloy structure of the as-synthesized Pd<sub>59</sub>Cu<sub>30</sub>Co<sub>11</sub> nanodendrites was further confirmed by aberration-corrected high-resolution elemental mapping analysis (Fig. 1d–h). The elemental mapping of Pd<sub>59</sub>Cu<sub>30</sub>Co<sub>11</sub>, showed that the Pd, Cu, and Co distributed throughout the whole particle (Fig. 1e–h). Simultaneously, the Pd, Cu, and Co atoms were verified to coexist in the topmost atomic layer within near-surface of the as-synthesized Pd<sub>59</sub>Cu<sub>30</sub>Co<sub>11</sub> nanodendrite and Pd atoms neighbored Cu and Co atoms. The aberration-corrected high-resolution TEM was further used to analyze the surface structure of the as-synthesized Pd<sub>59</sub>Cu<sub>30</sub>Co<sub>11</sub> nanodendrite. As shown in Fig. 2, abundant defects including low-coordination number (edges, corners, and steps) atoms, grain boundaries, lattice disorder, gap atoms, vacancies, and nanotwins were clearly observed in the surface. These defects have been confirmed to act as highly active sites and can boost the catalytic performance of catalysts in catalytic reaction<sup>4,19,47–51</sup>.

X-ray photoelectron spectroscopy (XPS) is generally accepted to analyze the surface composition and state of nanocrystal surface within 2.0 nm. The XPS results (Fig. 3) of the as-synthesized Pd<sub>59</sub>Cu<sub>30</sub>Co<sub>11</sub> showed that the Pd, Cu, and Co atoms coexisted in the near-surface of Pd<sub>59</sub>Cu<sub>30</sub>Co<sub>11</sub> nanoalloys. The binding energy of the Pd 3*d* peaks (Fig. 3a) shifted to 335.5 and 340.7 eV compared to the standard Pd 3*d* peaks (335.2 and 340.4 eV), and the binding energy of metallic Pd in the nanosurface of Pd<sub>59</sub>Cu<sub>30</sub>Co<sub>11</sub> nanoalloys positively shifted about 0.3 eV, which meant the downshift of the *d*-band center of Pd and this result was in accordance with aforementioned reports<sup>13,46,52,53</sup>. To further probe the local structure of the Pd<sub>59</sub>Cu<sub>30</sub>Co<sub>11</sub> nanoalloys at atomic scale, the X-ray absorption fine structure measurements were performed at the Pd K-edge. From the X-ray absorption

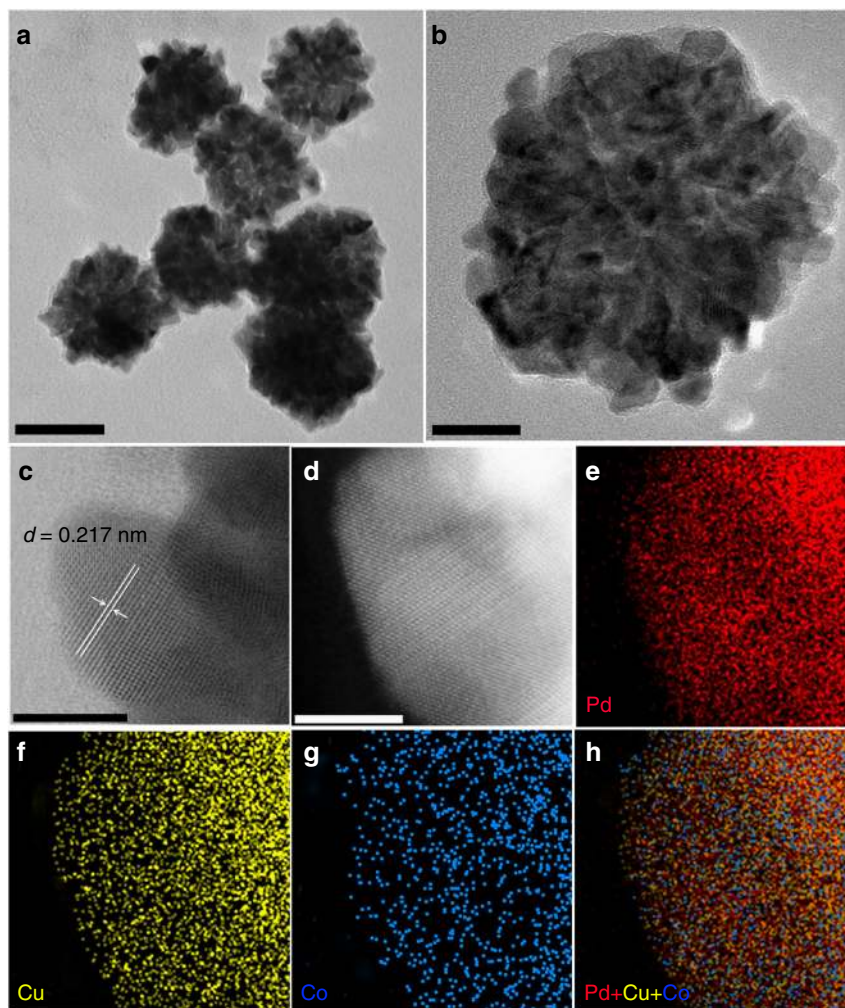


**Fig. 1** Characterization of the as-synthesized Pd<sub>59</sub>Cu<sub>30</sub>Co<sub>11</sub> nanoalloys. The typical transmission electron microscopy (TEM) (**a, b**), the high-resolution TEM (HRTEM) (**c**) images, the aberration-corrected high-resolution high-angle annular-dark field scanning transmission electron microscopy (HAADF-STEM) (**d**) images and the corresponding energy dispersive X-ray spectroscopy (EDS) elemental mapping (**e-h**) images of the as-synthesized Pd<sub>59</sub>Cu<sub>30</sub>Co<sub>11</sub> nanoalloys. (Scale bar: **a** is 50 nm, **b** is 20 nm, **c, d** are 5 nm.)

near edge structure of the Pd K-edge (Fig. 3d), we can clearly see that the Pd K-edge curve of the Pd<sub>59</sub>Cu<sub>30</sub>Co<sub>11</sub> nanoalloys was almost the same as that of metal state of Pd-foil and was quite different from that of the PdO, indicating that the as-synthesized Pd<sub>59</sub>Cu<sub>30</sub>Co<sub>11</sub> did not contain the PdO. The binding energy of Cu 2*p* peaks (Fig. 3b) negatively shifted to 931.9 and 951.9 eV compared to the standard Cu 2*p* peaks (932.6 and 952.56 eV). The binding energy of Co 2*p* peaks (Fig. 3c) showed a positive shift compared with the standard metallic Co peaks (778.3 and 793.2 eV), and the oxidized state Co also existed in the nanosurface of Pd<sub>59</sub>Cu<sub>30</sub>Co<sub>11</sub> nanoalloys. The shifts of binding energy could be ascribed to the strong electronic effects between Pd, Cu, and Co elements through *d*-band hybridization upon alloying within the atomic range<sup>12,13,40,41</sup>.

**ORR performance.** The ORR performance of the dendritic Pd<sub>59</sub>Cu<sub>30</sub>Co<sub>11</sub> nanoalloys have been investigated compared with commercial Pt/C, bimetallic Pd<sub>50</sub>Cu<sub>50</sub> and Pd<sub>88</sub>Co<sub>12</sub> and trimetallic Pd<sub>56</sub>Cu<sub>38</sub>Co<sub>6</sub> and Pd<sub>62</sub>Cu<sub>16</sub>Co<sub>22</sub> alloy nanodendrites (Supplementary Fig. 2, Supplementary Fig. 3, Supplementary Fig. 4, Supplementary Fig. 5, and Supplementary Table 1) obtained at the same synthetic method as the dendritic Pd<sub>59</sub>Cu<sub>30</sub>Co<sub>11</sub> nanoalloys in an O<sub>2</sub>-saturated 0.1 mol L<sup>-1</sup> (M) KOH solution with a scan rate of 10 mV s<sup>-1</sup> and a rotation rate of 1600 rpm at

room temperature. The ORR polarization curves of these samples are shown in Fig. 4a. The half-wave potentials of the Pd<sub>50</sub>Cu<sub>50</sub>, Pd<sub>88</sub>Co<sub>12</sub>, Pd<sub>59</sub>Cu<sub>30</sub>Co<sub>11</sub>, Pd<sub>56</sub>Cu<sub>38</sub>Co<sub>6</sub>, Pd<sub>62</sub>Cu<sub>16</sub>Co<sub>22</sub>, and commercial Pt/C catalysts are 0.86, 0.90, 0.91, 0.90, 0.89, and 0.87 V, respectively, which exhibited that the Pd<sub>59</sub>Cu<sub>30</sub>Co<sub>11</sub> nanoalloys had a greatly reduced ORR overpotential and indicated the superior activity. This was also confirmed by Tafel plots of these samples (Fig. 4a, inset). The positions of hydrogen adsorption/desorption peaks were often used to analyze the surface structure of electrocatalyst (Supplementary Fig. 6a). As can be seen, the hydrogen adsorption/desorption peaks on these samples located at different position, which meant the surface structure and active site of these electrocatalysts were quite different and would display different ORR performance. The electrochemically active surface area (ECSA), calculated from the results of CO-stripping (Supplementary Fig. 7) of Pd<sub>50</sub>Cu<sub>50</sub>, Pd<sub>88</sub>Co<sub>12</sub>, Pd<sub>59</sub>Cu<sub>30</sub>Co<sub>11</sub>, Pd<sub>56</sub>Cu<sub>38</sub>Co<sub>6</sub>, and Pd<sub>62</sub>Cu<sub>16</sub>Co<sub>22</sub> dendritic nanoalloys was around 37.9, 41.2, 58.7, 46.3, and 44.7 m<sup>2</sup> g<sup>-1</sup><sub>Pd</sub>, respectively. The ECSA of commercial Pt/C was 67.8 m<sup>2</sup> g<sup>-1</sup><sub>Pt</sub>. Figure 4b showed the specific activity (SA) and MA of ORR normalized by ECSA and Pd or Pt loading at 0.9 V versus a RHE using Koutecky–Levich equation, respectively. Among them, the Pd<sub>59</sub>Cu<sub>30</sub>Co<sub>11</sub> nanoalloys showed the best SA and MA. The SA and MA on the Pd<sub>59</sub>Cu<sub>30</sub>Co<sub>11</sub> nanoalloys were 0.90 mA cm<sup>-2</sup> and 0.38 A mg<sup>-1</sup><sub>Pd</sub>, respectively.

**Table 1** The X-ray diffraction (XRD) results of different samples

Samples	2 $\theta$ /degree (111)	Lattice parameter (1/Å)	Strain (%)
Pd crystal (JCPDS-46-1403) <sup>23</sup>	40.11	0.2226	-
Pd <sub>50</sub> Cu <sub>50</sub>	41.68	0.2262	1.62
Pd <sub>88</sub> Co <sub>12</sub>	40.15	0.2242	0.72
Pd <sub>56</sub> Cu <sub>38</sub> Co <sub>6</sub>	40.49	0.2283	2.56
Pd <sub>59</sub> Cu <sub>30</sub> Co <sub>11</sub>	40.21	0.2304	3.50
Pd <sub>62</sub> Cu <sub>16</sub> Co <sub>22</sub>	40.19	0.2273	2.11

The MA on Pd<sub>59</sub>Cu<sub>30</sub>Co<sub>11</sub> nanoalloys was 3.45 times higher than commercial Pt/C catalysts (0.11 A mg<sup>-1</sup><sub>Pt</sub>). Impressively, our Pd<sub>59</sub>Cu<sub>30</sub>Co<sub>11</sub> nanoalloys had a competitively high MA in comparison with previously reported non-Pt metal nanocatalysts (Supplementary Table 2) that is also superior to the recently reported PdCuCo anisotropic structure (0.18 A mg<sup>-1</sup><sub>Pd</sub>)<sup>40</sup> and spherical PdCuCo (0.13 A mg<sup>-1</sup><sub>Pd</sub>)<sup>43</sup>. Furthermore, at 0.875 and 0.8 V versus RHE (Fig. 4c, d), the Pd<sub>59</sub>Cu<sub>30</sub>Co<sub>11</sub> nanoalloys exhibited the largest ORR SA (1.73 mA cm<sup>-2</sup> at 0.875 V, 3.76 times that of commercial Pt/C; 10.20 mA cm<sup>-2</sup> at 0.8 V, 3.98 times that of commercial Pt/C) and MA (1.01 A mg<sup>-1</sup><sub>Pd</sub> at 0.875 V, 3.48 times that of commercial Pt/C; 5.98 A mg<sup>-1</sup><sub>Pd</sub> at 0.8 V, 3.71 times that of commercial Pt/C). Furthermore, in order to determine the electron transfer number on Pd<sub>59</sub>Cu<sub>30</sub>Co<sub>11</sub> nanoalloys, the ORR polarization curves of Pd<sub>59</sub>Cu<sub>30</sub>Co<sub>11</sub> nanoalloys were investigated by rotating disk electrode (RDE) measurements at different rotation rates from 400 to 2500 rpm in 0.1 M KOH solution (Supplementary Fig. 8a). The Koutecky–Levich (K–L) plots for Pd<sub>59</sub>Cu<sub>30</sub>Co<sub>11</sub> nanoalloys calculated at different potentials from 0.4 to 0.8 V were shown in Supplementary Fig. 8b. The slopes were parallel at different potentials, showing the first-order reaction kinetics and the electron transfer number was around four that indicated fully electrocatalytic reduction of oxygen into water on the Pd<sub>59</sub>Cu<sub>30</sub>Co<sub>11</sub> nanoalloys. The alcohol (methanol or ethanol) tolerance of the dendritic Pd<sub>59</sub>Cu<sub>30</sub>Co<sub>11</sub> nanoalloys was also investigated for ORR. Before testing ORR, the electrocatalytic activity toward methanol or ethanol of the dendritic Pd<sub>59</sub>Cu<sub>30</sub>Co<sub>11</sub> nanoalloys and commercial Pt/C were performed using cyclic voltammetry in 0.1 M KOH + 0.1 M methanol/ethanol solution. As shown in Fig. 5a–c, typical methanol and EO peaks were observed at 0.88 and 0.87 V, respectively, on commercial Pt/C, while methanol oxidation peak was hardly generated on the dendritic Pd<sub>59</sub>Cu<sub>30</sub>Co<sub>11</sub> nanoalloys and EO peak was only one-sixth of that on commercial Pt/C, which meant much lower electrocatalytic activity toward methanol and EO on the dendritic Pd<sub>59</sub>Cu<sub>30</sub>Co<sub>11</sub> nanoalloys compared with commercial Pt/C. The ORR polarization curves (Fig. 5b–d) showed the commercial Pt/C had a weak methanol and ethanol tolerance capacity. The half-wave potentials of the commercial Pt/C are 0.707 and 0.619 V versus RHE in the presence of methanol and ethanol, respectively, and the half-wave potentials negatively shifted 0.163 and 0.251 V, respectively, compared with that (0.87 V versus RHE; Fig. 4a) without methanol and ethanol. However, the dendritic Pd<sub>59</sub>Cu<sub>30</sub>Co<sub>11</sub> nanoalloys exhibited excellent methanol and ethanol tolerance capacity. The half-wave potential (0.91 V without methanol and ethanol; Fig. 4a) were barely affected by methanol (0.909 V versus RHE) and ethanol (0.907 V versus RHE). These results showed that the dendritic Pd<sub>59</sub>Cu<sub>30</sub>Co<sub>11</sub> nanoalloys had much better antimethanol and ethanol interference ability than the commercial Pt/C.

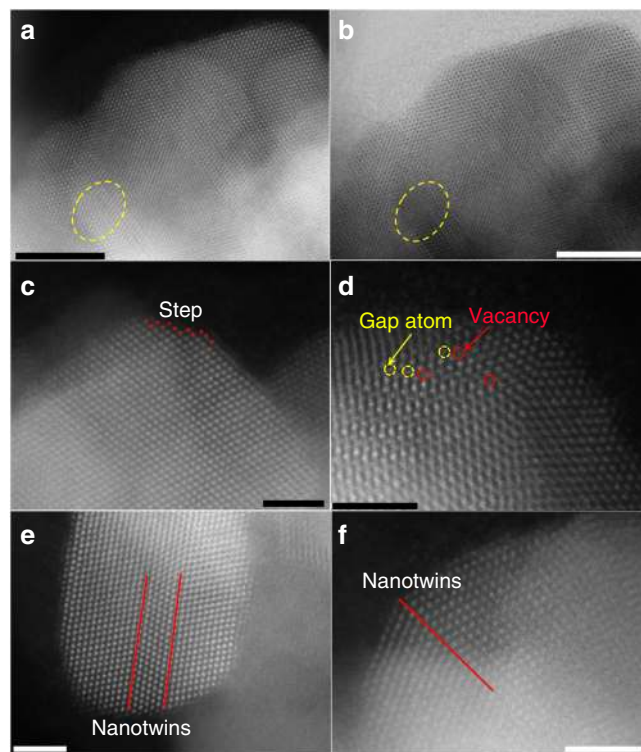


**Fig. 2** Surface defect characterization of the as-synthesized Pd<sub>59</sub>Cu<sub>30</sub>Co<sub>11</sub> nanoalloys. Defect analysis images of the as-synthesized dendritic Pd<sub>59</sub>Cu<sub>30</sub>Co<sub>11</sub> nanoalloys through aberration-corrected transmission electron microscopy (TEM). **a, b** Edge, corner and lattice disorder (in yellow dashed circle); **c** step; **d** gap atom in yellow dashed circle and vacancy in red dashed circle; **e, f** Nanotwins. (Scale bar: **a, b** are 5 nm, **c–f** are 2 nm.)

The dendritic Pd<sub>59</sub>Cu<sub>30</sub>Co<sub>11</sub> nanoalloys also presented long-term durability under the ORR reaction condition. The accelerated durability tests (ADTs) were used to evaluate ORR durability under a sweep rate of 100 mV s<sup>-1</sup> between 0.53 and 1.03 V in O<sub>2</sub>-saturated 0.1 M KOH solution. After 5000, 10,000, and 15,000 sweeping cycles, the MA of the Pd<sub>59</sub>Cu<sub>30</sub>Co<sub>11</sub> nanoalloy was 0.44, 0.40, and 0.26 A mg<sup>-1</sup><sub>Pd</sub>, respectively, at 0.9 V versus RHE (Fig. 4e–f), which first experienced a rise and then a drop. This could be ascribed to the surface structure change under the ADTs and the same phenomenon was also observed about trimetallic PtPdAu alloys reported by Ding's group<sup>54</sup>. However, the MA of Pt/C after 5000 and 10,000 sweeping cycles was 0.05 and 0.03 A mg<sup>-1</sup><sub>Pt</sub>, respectively, at 0.9 V versus RHE. After 10,000 sweeping cycles, the Pt/C catalyst shows the 72.7% loss of MA, while the Pd<sub>59</sub>Cu<sub>30</sub>Co<sub>11</sub> nanoalloys showed no loss of MA (0.40 A mg<sup>-1</sup><sub>Pd</sub>) that was 13.3 times higher than Pt/C. And after 15,000 sweeping cycles, the MA (0.26 A mg<sup>-1</sup><sub>Pd</sub>) of the Pd<sub>59</sub>Cu<sub>30</sub>Co<sub>11</sub> nanoalloys is 2.36 times higher than initial MA (0.11 A mg<sup>-1</sup><sub>Pt</sub>) of Pt/C and had a loss of 31.6% compared with the initial MA (0.38 A mg<sup>-1</sup><sub>Pd</sub>). The above results exhibited that the Pd<sub>59</sub>Cu<sub>30</sub>Co<sub>11</sub> nanoalloys had considerable enhancement with respect to durability compared with commercial Pt/C. After ADTs, we checked the morphologies of the Pd<sub>59</sub>Cu<sub>30</sub>Co<sub>11</sub> nanoalloys using TEM (Supplementary Fig. 9). The TEM images showed the Pd<sub>59</sub>Cu<sub>30</sub>Co<sub>11</sub> nanoalloys also maintained dendritic structure, however, after 15,000 sweeping cycles, the size of the small grains obviously increased due to the movement, aggregation and Ostwald ripening processes under the ADTs<sup>19</sup>, and we can clearly observe that some dendritic nanocrystals are hollow-like shapes, which caused by the electrochemical dealloying of Cu or Co (Supplementary Fig. 9), these were the reason why the

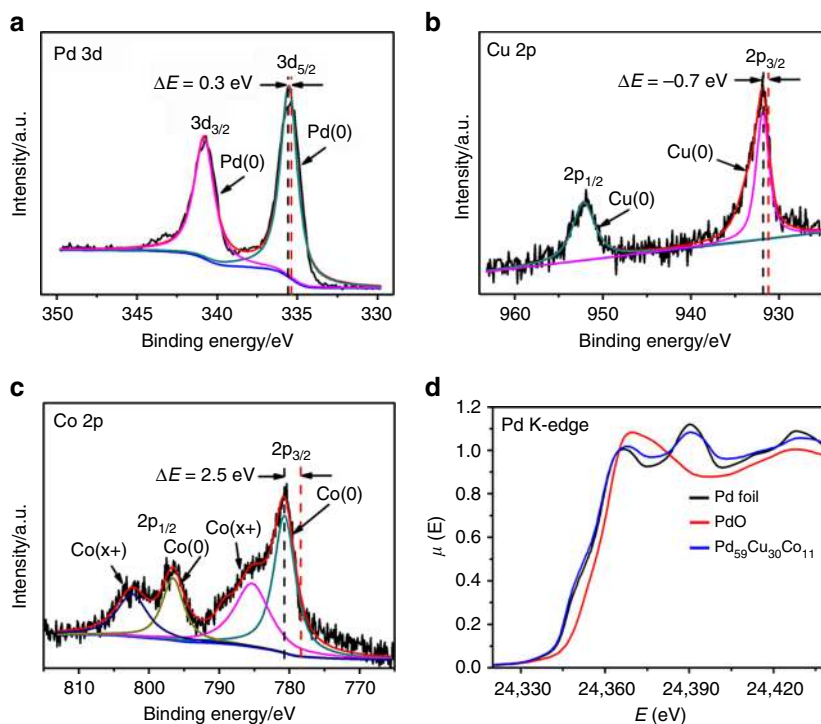


**Fig. 3** In-depth composition and structural analyses of the Pd<sub>59</sub>Cu<sub>30</sub>Co<sub>11</sub> nanoalloys. The X-ray photoelectron spectroscopy (XPS) spectra of the as-synthesized dendritic Pd<sub>59</sub>Cu<sub>30</sub>Co<sub>11</sub> nanoalloys **a** Pd 3d region, **b** Cu 2p region, **c** Co 2p region (the red dash lines in pictures indicate the standard positions of Pd 3d, Cu 2p and Co 2p), **d** the X-ray absorption near edge structure (XANES) spectra for the Pd K-edge

catalytic activity decreased. After ADT cycles, the composition of Pd<sub>59</sub>Cu<sub>30</sub>Co<sub>11</sub> nanoalloys changed (Supplementary Fig. 10). After 5000 cycles, the composition was 69.41 at% Pd, 29.29 at% Cu, and 1.30 at% Co. After 10,000 cycles, the composition was the 77.30 at% Pd, 21.78 at% Cu, and 0.92 at% Co, and after 15,000 cycles it was 83.68 at% Pd, 15.68 at% Cu and 0.64 at% Co. Moreover, the dendritic structure had stronger antiaggregation capacity due to their free-standing architectural feature than commercial Pt/C. For commercial Pt/C, after 10,000 cycles, the size of Pt particles obviously increased relative to initial size, namely, the size increased from sub-3.0 nm to around 10 nm (Supplementary Fig. 11), which led to the sharp fall of activity of commercial Pt/C.

**Formic acid oxidation performance.** The dendritic Pd<sub>59</sub>Cu<sub>30</sub>Co<sub>11</sub> nanoalloys also exhibited excellent FAO activity. Figure 6a showed that the SA of the Pd<sub>50</sub>Cu<sub>50</sub>, Pd<sub>88</sub>Co<sub>12</sub>, Pd<sub>56</sub>Cu<sub>38</sub>Co<sub>6</sub>, Pd<sub>59</sub>Cu<sub>30</sub>Co<sub>11</sub>, Pd<sub>62</sub>Cu<sub>16</sub>Co<sub>22</sub>, commercial Pd black, and Pt/C were around 6.38, 2.94, 7.25, 9.06, 6.46, 2.24, and 0.56 mA cm<sup>-2</sup>, respectively. The MA (Fig. 6b) of the Pd<sub>50</sub>Cu<sub>50</sub>, Pd<sub>88</sub>Co<sub>12</sub>, Pd<sub>56</sub>Cu<sub>38</sub>Co<sub>6</sub>, Pd<sub>59</sub>Cu<sub>30</sub>Co<sub>11</sub>, Pd<sub>62</sub>Cu<sub>16</sub>Co<sub>22</sub>, commercial Pd black, and Pt/C was 2.42, 1.21, 3.36, 5.32, 2.89, 0.39 A mg<sup>-1</sup><sub>Pd</sub> and 0.35 A mg<sup>-1</sup><sub>Pt</sub>, respectively. These values (Fig. 6c) showed that the as-synthesized Pd-based alloys displayed greatly enhanced activity compared with commercial Pd black and Pt/C. And the values of Pd<sub>59</sub>Cu<sub>30</sub>Co<sub>11</sub> nanoalloys were the largest. The FAO SA and MA of the Pd<sub>59</sub>Cu<sub>30</sub>Co<sub>11</sub> nanoalloys were 4.04 and 13.6 times higher than that of commercial Pd black, respectively, and 16.1 and 15.2 times higher than commercial Pt/C, respectively. Similar to the case of ORR, the Pd<sub>59</sub>Cu<sub>30</sub>Co<sub>11</sub> nanoalloys display high MA relative to previously reported Pd-based electrocatalysts (Supplementary Table 3). Moreover, the stability of the as-synthesized PdCuCo nanoalloys was evaluated by current–time curves and showed better stability than Pd<sub>50</sub>Cu<sub>50</sub>, Pd<sub>88</sub>Co<sub>12</sub>, commercial Pd black and Pt/C (Fig. 6d).

## Discussion

The excellent electrocatalytic performance of the as-synthesized dendritic Pd<sub>59</sub>Cu<sub>30</sub>Co<sub>11</sub> nanoalloys is mainly ascribed to the following reasons: (1) The special dendritic nanostructure of the Pd<sub>59</sub>Cu<sub>30</sub>Co<sub>11</sub> nanoalloy can provide abundant defects, such as low-coordination number atoms (edges, corners, and steps), grain boundaries, lattice disorder, nanotwins, gap atoms, and vacancies, which have been confirmed to boost the catalytic performance in catalytic reactions<sup>4,19,43,47–51</sup>. (2) Synergistic surface effects between Pd, Cu, and Co elements are present in the topmost atomic layer and favor the removal of poisoning intermediates (such as CO adsorbed (CO<sub>ads</sub>) and OH adsorbed (OH<sub>ads</sub>)) that are produced in the electrocatalytic reaction<sup>6,23,37,42</sup>. Moreover, metallic Cu and Co have been found to constitute sites for activating oxygen, water or small organic molecules and improve the activity and durability in FCs<sup>13,23,54–62</sup>. (3) Pd alloying with Cu and Co changes the surface electronic structure through ligand effect and downshifts the *d*-band center of Pd, which can tune the adsorption/desorption capacities of activating reactant molecules or intermediates and enhance the catalytic performance<sup>39,40,43</sup>. (4) Strain effects have also been shown to contribute to high catalytic performance<sup>7,10,12,60–62</sup>. The surface strain in dendritic Pd<sub>59</sub>Cu<sub>30</sub>Co<sub>11</sub> nanoalloys may be attributed to the lattice mismatch triggered by the incorporation of smaller Cu and Co atoms into the Pd *fcc* lattice, small size of sub-5.0 nm grains that construct the dendritic structure and a boundary that originates from the mutual cross-linking of small grains<sup>59,60</sup>.

In conclusion, the defect-rich dendritic PdCuCo nanoalloys have been synthesized by a facile one-pot method to be developed as high-performance non-Pt nanocatalysts toward ORR and FAO. Among them, a Pd<sub>59</sub>Cu<sub>30</sub>Co<sub>11</sub> nanoalloy shows the best catalytic performances. For ORR, the SA (0.90 mA cm<sup>-2</sup> at 0.9 V and 1.73 mA cm<sup>-2</sup> at 0.875 V versus RHE) and MA (0.38 A mg<sup>-1</sup><sub>Pd</sub> at 0.9 V versus RHE and 1.01 A mg<sup>-1</sup><sub>Pd</sub> at 0.875 V versus RHE) of the dendritic Pd<sub>59</sub>Cu<sub>30</sub>Co<sub>11</sub> nanoalloy are 2.19 and 3.76 times and

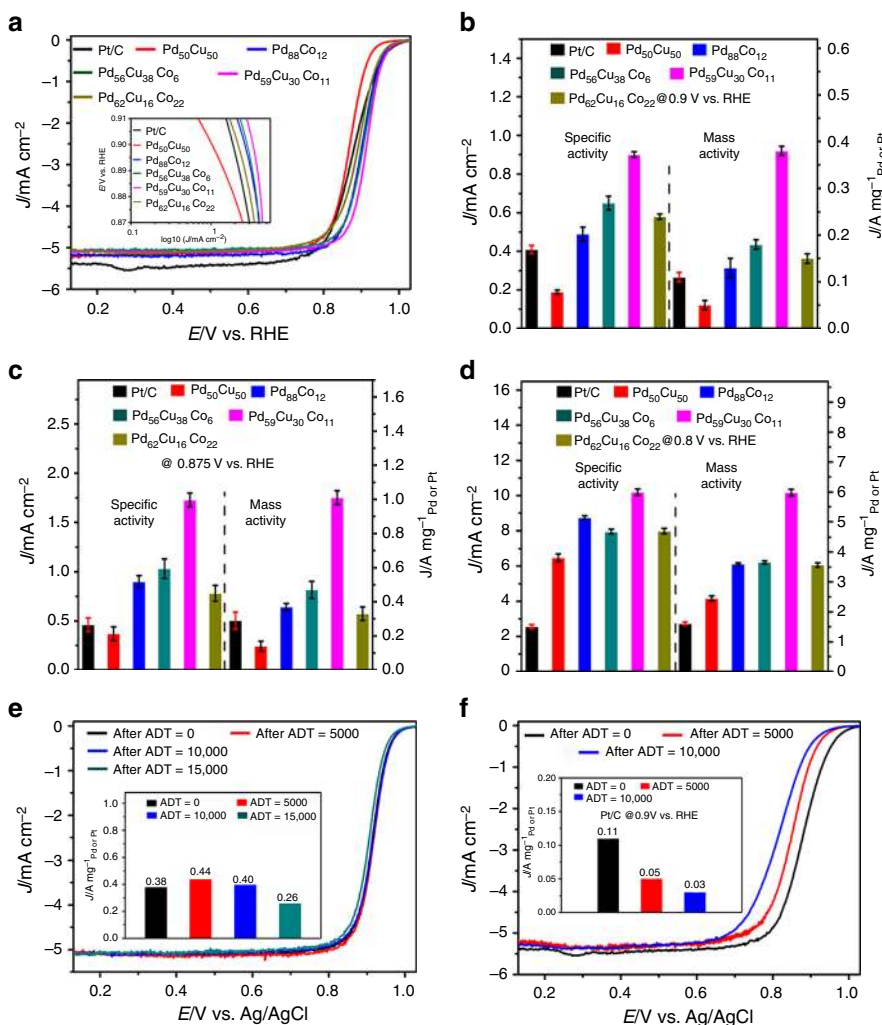


**Fig. 4** Oxygen reduction reaction performance characterization. The oxygen reduction reaction (ORR) performance of Pt/C, Pd<sub>88</sub>Co<sub>12</sub>, Pd<sub>50</sub>Cu<sub>50</sub>, Pd<sub>56</sub>Cu<sub>38</sub>Co<sub>6</sub>, Pd<sub>59</sub>Cu<sub>30</sub>Co<sub>11</sub>, and Pd<sub>62</sub>Cu<sub>16</sub>Co<sub>22</sub> catalysts. **a** The ORR polarization curves were recorded in O<sub>2</sub>-saturated 0.1 mol L<sup>-1</sup> (M) potassium hydroxide (KOH) and the inset was the corresponding specific activity Tafel plots. Histograms of ORR specific activities and mass activities of the Pt/C, Pd<sub>88</sub>Co<sub>12</sub>, Pd<sub>50</sub>Cu<sub>50</sub>, Pd<sub>56</sub>Cu<sub>38</sub>Co<sub>6</sub>, Pd<sub>59</sub>Cu<sub>30</sub>Co<sub>11</sub>, and Pd<sub>62</sub>Cu<sub>16</sub>Co<sub>22</sub> catalysts at 0.9 V (**b**), 0.875 V (**c**), and 0.8 V (**d**) versus reversible hydrogen electrode (RHE). **e, f** The ORR polarization curves for the Pd<sub>59</sub>Cu<sub>30</sub>Co<sub>11</sub> and commercial Pt/C catalysts before and after cycles of accelerated durability tests (ADTs) (the inset was the corresponding mass activity at 0.90 V versus RHE). Error bars are  $\pm$ s.d.

3.45 and 3.48 times those of commercial Pt/C, respectively. The long-term durability has been evaluated through an ADT. After 10,000 cycles, the commercial Pt/C catalyst shows the 72.7% loss of MA, while the Pd<sub>59</sub>Cu<sub>30</sub>Co<sub>11</sub> nanoalloy showed no loss of MA. After 15,000 cycles, the MA (0.26 A mg<sup>-1</sup><sub>Pd</sub>) of the Pd<sub>59</sub>Cu<sub>30</sub>Co<sub>11</sub> nanoalloy is 2.36 times higher than initial MA (0.11 A mg<sup>-1</sup><sub>Pt</sub>) of Pt/C. For FAO, the SA and MA of the Pd<sub>59</sub>Cu<sub>30</sub>Co<sub>11</sub> nanoalloy is 4.04 and 13.6 times higher, respectively, than commercial Pd black and 16.1 and 15.2 times higher, respectively, than commercial Pt/C. The current–time curves show that the Pd<sub>59</sub>Cu<sub>30</sub>Co<sub>11</sub> nanoalloy exhibits better stability than commercial Pd black and Pt/C. And the dendritic Pd<sub>59</sub>Cu<sub>30</sub>Co<sub>11</sub> nanoalloy has good methanol/ethanol tolerance ability. Thus, this work provides an example of the development of a new type of robust multifunctional, non-Pt catalysts for FCs.

## Methods

**Synthesis of dendritic Pd<sub>59</sub>Cu<sub>30</sub>Co<sub>11</sub> nanoalloys.** The dendritic Pd<sub>59</sub>Cu<sub>30</sub>Co<sub>11</sub> nanoalloys were prepared by using precursors of Na<sub>2</sub>PdCl<sub>4</sub>, CuCl<sub>2</sub>, and CoCl<sub>2</sub>. Firstly, the 0.25 mL of 0.1 M Na<sub>2</sub>PdCl<sub>4</sub>, 0.125 mL of 0.1 M of 0.1 M of CuCl<sub>2</sub>, and 0.125 mL of 0.1 M of CoCl<sub>2</sub> were added to 8.8 mL of ethylene glycol containing

0.050 g polyvinyl pyrrolidone (PVP-8000), and stirred for 1–2 min then the yellow clear solution was obtained. Secondly, the 0.2 mL ammonium hydroxide was added to the above solution, and stirred for 30 min. Then, the resulting clear solution was transferred to a 15-mL Teflon-lined stainless-steel autoclave. The oven was then heated at 150 °C for 8 h, then the Teflon-lined stainless-steel autoclave was taken out after it was cooled to room temperature. The products were separated several times by centrifugation and washing cycles at 10,000 rpm for 15 min with ethanol. The Pd<sub>59</sub>Cu<sub>30</sub>Co<sub>11</sub> was redispersed in ethanol. By adjusting the ratio of Cu or Co precursors, the Pd<sub>50</sub>Cu<sub>50</sub>, Pd<sub>88</sub>Co<sub>12</sub>, Pd<sub>56</sub>Cu<sub>38</sub>Co<sub>6</sub>, and Pd<sub>62</sub>Cu<sub>16</sub>Co<sub>22</sub> nanoalloys can be obtained under the same procedure. Further details are provided in the Supplementary Methods.

**The ORR electrochemical measurement.** For the ORR electrochemical measurement, a glassy carbon RDE (PINE, USA) was used. A Hg/HgO (0.1 M KOH) electrode and Pt black plate were used as reference and counter electrodes, respectively. The ORR was performed in the O<sub>2</sub>-saturated 0.1 M KOH solution at room temperature. Then, using a glassy carbon RDE at a rotation rate of 1600 rpm, the potential was scanned from 0.13 to 1.03 V (versus RHE) at a scan rate of 10 mV s<sup>-1</sup> and were corrected for capacitive currents in N<sub>2</sub> saturation. The kinetic current (*i<sub>k</sub>*) can be derived from the experimental data using the well-known Koutecky–Levich equation:  $(1/i_k = 1/i - 1/i_L)$  at 0.90 V versus RHE, where *i<sub>L</sub>* and *i* are the diffusion limiting current and measured current (0.90 V versus RHE) at kinetic-diffusion control region, respectively.

The tolerance test: A Hg/HgO (0.1 M KOH) electrode and Pt black plate were used as reference and counter electrodes, respectively. Then MOR or EOR tested

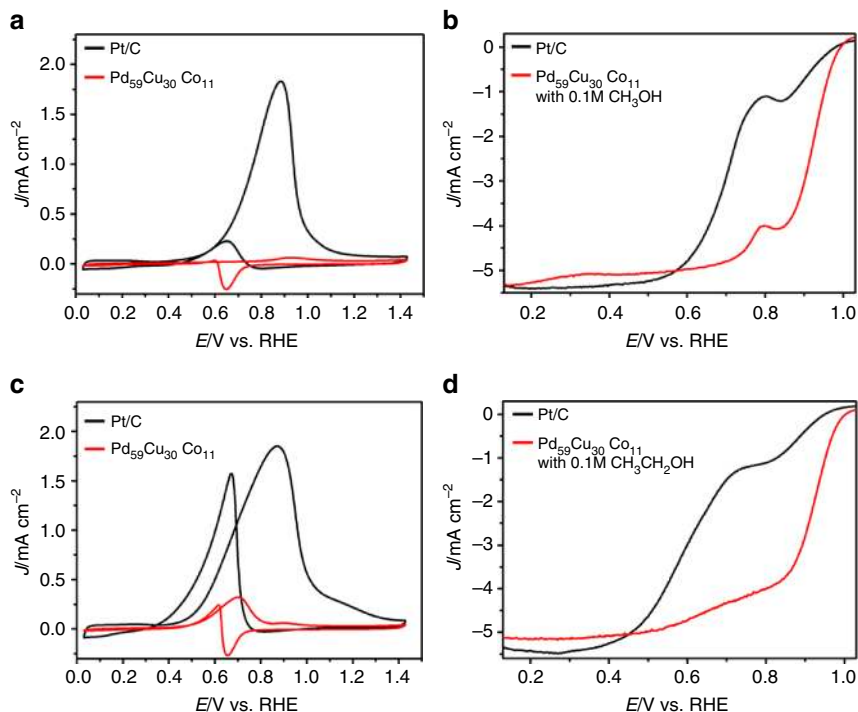


**Fig. 5** Methanol and ethanol tolerance tests. Cyclic voltammetry (CV) curves of the dendritic Pd<sub>59</sub>Cu<sub>30</sub>Co<sub>11</sub> nanoalloys and the commercial Pt/C in N<sub>2</sub>-saturated 0.1 mol L<sup>-1</sup> (M) potassium hydroxide (KOH) + 0.1 M methanol (CH<sub>3</sub>OH) (a) or ethanol (CH<sub>3</sub>CH<sub>2</sub>OH) (c) solution at 50 mV s<sup>-1</sup>. Oxygen reduction reaction (ORR) polarization curves of the dendritic Pd<sub>59</sub>Cu<sub>30</sub>Co<sub>11</sub> nanoalloys and the commercial Pt/C in O<sub>2</sub>-saturated 0.1 M KOH + 0.1 M methanol (b) or ethanol (d) solution at 10 mV s<sup>-1</sup> and rotation rate of 1600 rpm

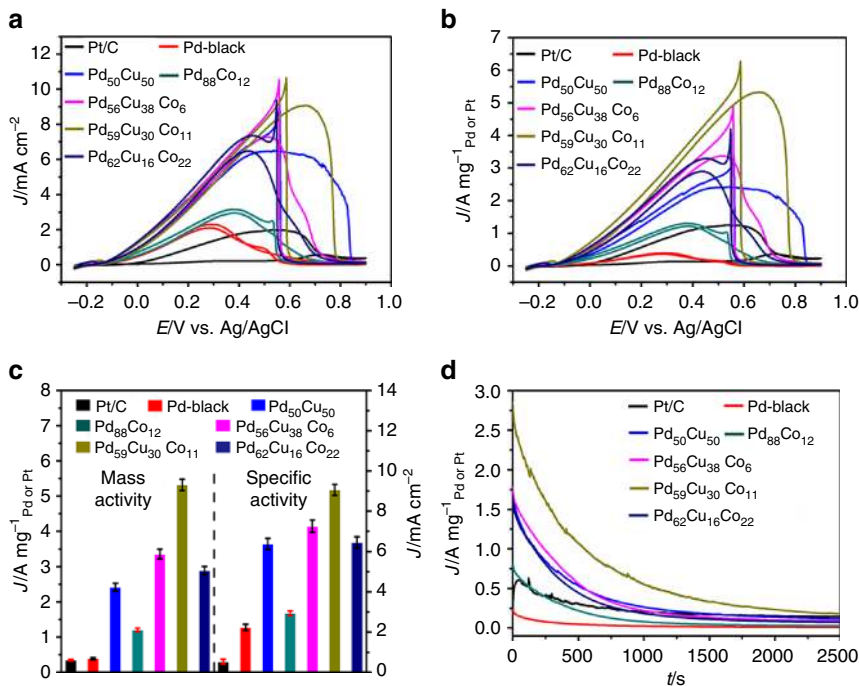


**Fig. 6** Formic acid oxidation (FAO) characterization. Cyclic voltammetry (CV) curves (specific activity (a) and mass activity (b)) of the as-synthesized Pd<sub>50</sub>Cu<sub>50</sub>, Pd<sub>88</sub>Co<sub>12</sub>, Pd<sub>56</sub>Cu<sub>38</sub>Co<sub>6</sub>, Pd<sub>59</sub>Cu<sub>30</sub>Co<sub>11</sub>, Pd<sub>62</sub>Cu<sub>16</sub>Co<sub>22</sub>, commercial Pt/C, and Pd black with a scan rate of 50 mV s<sup>-1</sup> in 0.1 mol L<sup>-1</sup> (M) perchloric acid (HClO<sub>4</sub>) + 0.5 M formic acid (HCOOH) solution at room temperature. c Histograms of formic acid oxidation (FAO) specific activity and mass activity. Error bars are  $\pm$ s.d. d Current-time curves of the as-synthesized Pd<sub>50</sub>Cu<sub>50</sub>, Pd<sub>88</sub>Co<sub>12</sub>, Pd<sub>56</sub>Cu<sub>38</sub>Co<sub>6</sub>, Pd<sub>59</sub>Cu<sub>30</sub>Co<sub>11</sub>, Pd<sub>62</sub>Cu<sub>16</sub>Co<sub>22</sub>, commercial Pt/C, and Pd black recorded at 0.25 V for 2500 s in 0.1 M HClO<sub>4</sub> + 0.5 M HCOOH solution at room temperature

with a scan rate of  $50 \text{ mV s}^{-1}$  at room temperature in  $0.1 \text{ M KOH} + 0.1 \text{ M CH}_3\text{OH}$  or  $0.1 \text{ M KOH} + 0.1 \text{ M CH}_3\text{CH}_2\text{OH}$ , and the potential was scanned from 0.03 to 1.43 V (versus RHE), after this, using RDE at a rotation rate of 1600 rpm, and the potential was scanned from 0.13 to 1.03 V (versus RHE) at a scan rate of  $10 \text{ mV s}^{-1}$ .

### Data availability

All relevant data are available from the corresponding author upon reasonable request.

Received: 4 February 2018 Accepted: 13 August 2018

Published online: 12 September 2018

### References

1. Steele, B. C. & Heinzel, A. Materials for fuel cell technologies. *Nature* **414**, 345–352 (2001).
2. Othman, R., Dicks, A. L. & Zhu, Z. Nonprecious metal catalysts for the PEM fuel cell cathode. *Int. J. Hydrogen Energy* **37**, 357–372 (2012).
3. Chen, A. & Holthindl, P. Platinum-based nanostructured materials: synthesis, properties, and applications. *Chem. Rev.* **110**, 3767–3804 (2010).
4. Zhang, Z. et al. One-pot synthesis of highly anisotropic fivefold-twinned PtCu nanoframes used as a bifunctional electrocatalyst for oxygen reduction and methanol oxidation. *Adv. Mater.* **28**, 8712–8717 (2016).
5. Zhang, N. et al. Superior bifunctional liquid fuel oxidation and oxygen reduction electrocatalysis enabled by PtNiPd core-shell nanowires. *Adv. Mater.* **29**, 1603774 (2016).
6. Liu, T. et al. Monodispersed sub-5.0 nm PtCu nanoalloys as enhanced bifunctional electrocatalysts for oxygen reduction reaction and ethanol oxidation reaction. *Nanoscale* **9**, 2963–2968 (2017).
7. Huang, X. et al. High-performance transition metal-doped Pt<sub>3</sub>Ni octahedra for oxygen reduction reaction. *Science* **348**, 1230–1234 (2015).
8. Casado-Rivera, E. et al. Electrochemical activity of ordered intermetallic phases for fuel cell applications. *J. Am. Chem. Soc.* **126**, 4043–4049 (2004).
9. Wang, Y. et al. Carbon-supported Pt-based alloy electrocatalysts for the oxygen reduction reaction in polymer electrolyte membrane fuel cells: particle size, shape, and composition manipulation and their impact to activity. *Chem. Rev.* **115**, 3433–3467 (2015).
10. Bianchini, C. & Shen, P. K. ChemInform abstract: palladium-based electrocatalysts for alcohol oxidation in half cells and in direct alcohol fuel cells. *Chem. Rev.* **109**, 4183–4206 (2009).
11. Antolini, E. Palladium in fuel, cell catalysis. *Energy Environ. Sci.* **2**, 915–931 (2009).
12. Suo, Y., Zhuang, L. & Lu, J. First-principles considerations in the design of Pd alloy catalysts for oxygen reduction. *Angew. Chem. Int. Ed.* **46**, 2862–2864 (2007).
13. Maheswari, S., Karthikeyan, S., Murugan, P., Sridhar, P. & Pitchumani, S. Carbon-supported Pd–Co as cathode catalyst for APEMFCs and validation by DFT. *Phys. Chem. Chem. Phys.* **14**, 9683–9695 (2012).
14. Holewinski, A., Idrobo, J. C. & Linic, S. High-performance Ag–Co alloy catalysts for electrochemical oxygen reduction. *Nat. Chem.* **6**, 828–834 (2014).
15. Ahn, M. et al. Rhodium–tin binary nanoparticle-a strategy to develop an alternative electrocatalyst for oxygen reduction. *ACS Catal.* **7**, 5796–5801 (2017).
16. Narayanamoorthy, B. et al. Enhanced intrinsic activity and stability of Au–Rh bimetallic nanostructures as a supportless cathode electrocatalyst for oxygen reduction in alkaline fuel cells. *ACS Sustain. Chem. Eng.* **4**, 6480–6490 (2016).
17. Yan, Y. et al. Kinetically controlled growth of cubic and octahedral Rh–Pd alloy oxygen reduction electrocatalysts with high activity and durability. *Nanoscale* **7**, 301–307 (2015).
18. Qi, Y. Wu et al. Facile synthesis of Rh–Pd alloy nanodendrites as highly active and durable electrocatalysts for oxygen reduction reaction. *Nanoscale* **6**, 7012–7018 (2014).
19. Li, M. et al. Ultrafine jagged platinum nanowires enable ultrahigh mass activity for the oxygen reduction reaction. *Science* **354**, 1414–1419 (2016).
20. Wang, X., Yang, J., Yi, H., Song, R. & Tang, Z. “Raisin bun”-like nanocomposites of palladium clusters and porphyrin for superior formic acid oxidation. *Adv. Mater.* **25**, 2728–2732 (2013).
21. Feng, L. et al. Nanostructured palladium catalyst poisoning depressed by cobalt phosphide in the electrooxidation of formic acid for fuel cells. *Nano Energy* **30**, 355–361 (2016).
22. Wang, C., Chen, D. P., Sang, X., Unocic, R. R. & Skrabalak, S. E. Size-dependent disorder–order transformation in the synthesis of monodisperse intermetallic PdCu nanocatalysts. *ACS Nano* **10**, 6345–6353 (2016).
23. Zhang, L. et al. Pd–Cu bimetallic tripods: a mechanistic understanding of the synthesis and their enhanced electrocatalytic activity for formic acid oxidation. *Adv. Funct. Mater.* **24**, 7520–7529 (2015).
24. Chen, Y. et al. High-yield synthesis of crystal-phase-heterostructured 4H/fcc Au@Pd core-shell nanorods for electrocatalytic ethanol oxidation. *Adv. Mater.* **29**, 1701331 (2017).
25. Dai, Y. et al. Carbon monoxide-assisted synthesis of single-crystalline Pd tetrapod nanocrystals through hydride formation. *J. Am. Chem. Soc.* **134**, 7073–7080 (2012).
26. Du, C., Chen, M., Wang, W. & Yin, G. Nanoporous PdNi alloy nanowires as highly active catalysts for the electrooxidation of formic acid. *ACS Appl. Mater. Interfaces* **3**, 105–109 (2011).
27. Lu, Y., Jiang, Y., Gao, X., Wang, X. & Chen, W. Strongly coupled Pd nanotetrahedron/tungsten oxide nanosheet hybrids with enhanced catalytic activity and stability as oxygen reduction electrocatalysts. *J. Am. Chem. Soc.* **136**, 11687–11697 (2014).
28. Jiang, R., Tran, McClure, D. T. J. P. & Chu, D. A class of (Pd–Ni–P) electrocatalysts for the ethanol oxidation reaction in alkaline media. *ACS Catal.* **4**, 2577–2586 (2014).
29. Jin, M., Zhang, H., Xie, Z. & Xia, Y. Palladium concave nanocubes with high-index facets and their enhanced catalytic properties. *Angew. Chem. Int. Ed.* **123**, 7850–7854 (2011).
30. Zhou, Z., Kang, X., Song, Y. & Chen, S. Butylphenyl-functionalized palladium nanoparticles as effective catalysts for the electrooxidation of formic acid. *Chem. Commun.* **47**, 6075–6077 (2011).
31. Huang, X. et al. Free-standing palladium nanosheets with plasmonic and catalytic properties. *Nat. Nanotech.* **6**, 28–32 (2011).
32. Chen, L. et al. Nanoporous PdNi bimetallic catalyst with enhanced electrocatalytic performances for electrooxidation and oxygen reduction reactions. *Adv. Funct. Mater.* **21**, 4364–4370 (2011).
33. Mazumder, V., MoreK. L. & SunS. et al. A facile synthesis of MPd (M = Co, Cu) nanoparticles and their catalysis for cormic acid oxidation. *Nano Lett.* **12**, 1102–1106 (2012).
34. Ghosh, A., Chandran, P. & Ramaprabhu, S. Palladium–nitrogen coordinated cobalt alloy toward hydrogen oxidation and oxygen reduction reactions with high catalytic activity in renewable energy generations of proton exchange membrane fuel cell. *Appl. Energy* **208**, 37–48 (2017).
35. Koenigsmann, C. & Wong, S. S. Tailoring chemical composition to achieve enhanced methanol oxidation reaction and methanol-tolerant oxygen reduction reaction performance in palladium-based nanowire systems. *ACS Catal.* **3**, 2031–2040 (2013).
36. Guo, C. X., Zhang, L. Y., Miao, J., Zhang, J. & Li, C. M. DNA-functionalized graphene to guide growth of highly active Pd nanocrystals as efficient electrocatalyst for direct formic acid fuel cells. *Adv. Energy Mater.* **3**, 167–171 (2013).
37. Zheng, Y. et al. Component-controlled synthesis and assembly of Cu–Pd nanocrystals on graphene for oxygen reduction reaction. *ACS Appl. Mater. Interfaces* **7**, 5347–5357 (2015).
38. Zhang, Y. et al. Seedless growth of palladium nanocrystals with tunable structures: from tetrahedra to nanosheets. *Nano Lett.* **15**, 7519–7525 (2015).
39. Yang, N. et al. Synthesis of ultrathin PdCu alloy nanosheets used as a highly efficient electrocatalyst for formic acid oxidation. *Adv. Mater.* **29**, 1700769 (2017).
40. Zuo, Y. et al. Atomic vacancies control of Pd-based catalysts for enhanced electrochemical performance. *Adv. Mater.* **30**, 1704171 (2018).
41. Liu, H., Koenigsmann, C., Adzic, R. R. & Wong, S. S. Probing ultrathin one-dimensional Pd–Ni nanostructures as oxygen reduction reaction catalysts. *ACS Catal.* **4**, 2544–2555 (2014).
42. Liu, H., Zheng, Y., Wang, G. & Qiao, S. Z. A three-component nanocomposite with synergistic reactivity for oxygen reduction reaction in alkaline solution. *Adv. Energy Mater.* **5**, 618–622 (2015).
43. Jiang, K. et al. Ordered PdCu-based nanoparticles as bifunctional oxygen reduction and ethanol-oxidation electrocatalysts. *Angew. Chem. Int. Ed.* **55**, 9030–9035 (2016).
44. Wang, R. et al. One-pot solvothermal synthesis of PdCu nanocrystals with enhanced electrocatalytic activity toward glycerol oxidation and hydrogen evolution. *Int. J. Hydrogen Energy* **42**, 6695–6704 (2017).
45. Dai, Q. & Tang, J. The optical and magnetic properties of CoO and Co nanocrystals prepared by a facile technique. *Nanoscale* **5**, 7512–7519 (2013).
46. Xiao, W. et al. Optimizing the ORR activity of Pd-based nanocatalysts by tuning their strain and particle size. *J. Mater. Chem. A* **5**, 9867–9872 (2017).
47. Zhao, W. et al. Highly active and durable Pt<sub>72</sub>Ru<sub>28</sub> porous nanoalloy assembled with sub-4.0 nm particles for methanol oxidation. *Adv. Energy Mater.* **7**, 1601593 (2017).
48. Zhang, N. et al. Oxide defect engineering enables to couple solar energy into oxygen activation. *J. Am. Chem. Soc.* **138**, 8928–8935 (2016).
49. Lan, J., Wang, K., Yuan, Q. & Wang, X. Composition-controllable synthesis of defect-rich PtPdCu nanoalloys with hollow cavities as superior electrocatalysts for alcohol oxidation. *Mater. Chem. Front.* **1**, 1217–1222 (2017).
50. Xu, G. et al. Morphological and interfacial control of platinum nanostructures for electrocatalytic oxygen reduction. *ACS Catal.* **6**, 5260–5267 (2016).



51. Lim, B. et al. Pd–Pt bimetallic nanodendrites with high activity for oxygen reduction. *Science* **324**, 1302–1305 (2009).
52. Xue, Ha et al. Fabrication of PdCo bimetallic nanoparticles anchored on three-dimensional ordered N-doped porous carbon as an efficient catalyst for oxygen reduction reaction. *ACS Appl. Mater. Interfaces* **8**, 20766–20771 (2016).
53. Wang, A. et al. Palladium–cobalt nanotube arrays supported on carbon fiber cloth as high-performance flexible electrocatalysts for ethanol oxidation. *Angew. Chem. Int. Ed.* **54**, 3669–3673 (2015).
54. Li, J. et al. Surface evolution of a Pt–Pd–Au electrocatalyst for stable oxygen reduction. *Nat. Energy* **2**, 17111 (2017).
55. Fernández, J. L., Walsh, D. A. & Bard, A. J. Thermodynamic guidelines for the design of bimetallic catalysts for oxygen electroreduction and rapid screening by scanning electrochemical microscopy. M–Co (M: Pd, Ag, Au). *J. Am. Chem. Soc.* **127**, 357–365 (2005).
56. Chen, B., Cheng, D. & Zhu, J. Synthesis of PtCu nanowires in nonaqueous solvent with enhanced activity and stability for oxygen reduction reaction. *J. Power Sources* **267**, 380–387 (2014).
57. Huang, S., Yang, N., Wang, S., Sun, Y. & Zhu, Y. Tuning the synthesis of platinum–copper nanoparticles with a hollow core and porous shell for the selective hydrogenation of furfural to furfuryl alcohol. *Nanoscale* **8**, 14104–14108 (2014).
58. Chen, S., Su, H., Wang, Y., Wu, W. & Zeng, J. Size-controlled synthesis of platinum–copper hierarchical trigonal bipyramid nanoframes. *Angew. Chem. Int. Ed.* **54**, 108–113 (2015).
59. Bu, L. et al. Biaxially strained PtPb/Pt core/shell nanoplate boosts oxygen reduction catalysis. *Science* **354**, 1410–1414 (2016).
60. Wu, J. et al. Surface lattice-engineered bimetallic nanoparticles and their catalytic properties. *Chem. Soc. Rev.* **41**, 8066–8074 (2012).
61. Stamenkovic, V. R. et al. Trends in electrocatalysis on extended and nanoscale Pt–bimetallic alloy surfaces. *Nat. Mater.* **6**, 241–247 (2007).
62. Mavrikakis, M., Hammer, B. & Nørskov, J. K. Effect of strain on the reactivity of metal surfaces. *Phys. Rev. Lett.* **81**, 2819–2822 (1998).

## Acknowledgments

This work was supported by the National Natural Science Foundation of China (21571038, 21361005, 21431003, and 21521091), National Key R&D Program of China (2017YFA0700101 and 2016YFA0202801), the Open Fund of the Key Lab of Organic Optoelectronics & Molecular Engineering (Tsinghua University) and State Key

Laboratory of Physical Chemistry of Solid Surfaces (201520). We also thank Professor Zhi-You Zhou (Xiamen University) for the help of ORR experiments and discussion.

## Author contributions

C.L. synthesized the catalysts, prepared the fuel cell test materials and performed electrocatalytic tests. C.L., B.N., T.H., S.Z., Y.L., and L.G. performed the structure characterizations (TEM, HRTEM, ICP, XPS, XRD, and EDS). Q.Y. and X.W. wrote and edited the manuscript and Supplementary information. All authors contributed to discussions about the results and the manuscript. The project was conceived and supervised by Q.Y. and X.W.

## Additional information

**Supplementary Information** accompanies this paper at <https://doi.org/10.1038/s41467-018-06043-1>.

**Competing interests:** The authors declare no competing interests.

**Reprints and permission** information is available online at <http://npg.nature.com/reprintsandpermissions/>

**Publisher's note:** Springer Nature remains neutral with regard to jurisdictional claims in published maps and institutional affiliations.



**Open Access** This article is licensed under a Creative Commons Attribution 4.0 International License, which permits use, sharing, adaptation, distribution and reproduction in any medium or format, as long as you give appropriate credit to the original author(s) and the source, provide a link to the Creative Commons license, and indicate if changes were made. The images or other third party material in this article are included in the article's Creative Commons license, unless indicated otherwise in a credit line to the material. If material is not included in the article's Creative Commons license and your intended use is not permitted by statutory regulation or exceeds the permitted use, you will need to obtain permission directly from the copyright holder. To view a copy of this license, visit <http://creativecommons.org/licenses/by/4.0/>.

© The Author(s) 2018